

Article

Effective Removal of Methylene Blue by Mn_3O_4/NiO Nanocomposite under Visible Light

Komal Majeed ¹, Jaweria Ambreen ^{1,*}, Saeed Ahmed Khan ², Saz Muhammad ³, Aqeel Ahmed Shah ⁴, Muhammad Ali Bhatti ⁵, Syeda Sitwat Batool ⁶, Muhammad Farooq ⁷, Syed Nizam Uddin Shah Bukhari ⁸, Ali Dad Chandio ⁴, Sadaf Jamal Gilani ⁹ and May Nasser Bin Jumah ^{10,11,12}

- ¹ Department of Chemistry, COMSATS University Islamabad, Park Road, Islamabad 45550, Pakistan
 - ² Department of Electrical Engineering, Sukkur IBA University, Sukkur 65200, Pakistan
 - ³ Department of Chemistry, Lahore Garrison University, DHA Phase VI, Lahore 54792, Pakistan
 - ⁴ Wet Chemistry Laboratory, Department of Metallurgical Engineering, NED University of Engineering and Technology, University Road, Karachi 75720, Pakistan
 - ⁵ Institute of Environmental Sciences, University of Sindh Jamshoro, Jamshoro 76080, Pakistan
 - ⁶ Department of Physics, COMSATS University Islamabad, Park Road, Islamabad 45550, Pakistan; sitwatnaqvi@comsats.edu.pk
 - ⁷ Pakistan Council of Scientific and Industrial Research (PCSIR), PCSIR Head Office, 01-Constitution Avenue, Sector G-5/2, Islamabad 44000, Pakistan
 - ⁸ Department of Basic Science and Humanities, Dawood University of Engineering and Technology, Karachi 74800, Pakistan
 - ⁹ Department of Basic Health Sciences, Foundation Year, Princess Nourah bint Abdulrahman University, Riyadh 11671, Saudi Arabia
 - ¹⁰ Biology Department, College of Science, Princess Nourah bint Abdulrahman University, Riyadh 11671, Saudi Arabia
 - ¹¹ Environment and Biomaterial Unit, Health Sciences Research Center, Princess Nourah bint Abdulrahman University, Riyadh 11671, Saudi Arabia
 - ¹² Saudi Society for Applied Science, Princess Nourah bint Abdulrahman University, Riyadh 11671, Saudi Arabia
- * Correspondence: jaweria.ambreen@comsats.edu.pk



Citation: Majeed, K.; Ambreen, J.; Khan, S.A.; Muhammad, S.; Shah, A.A.; Bhatti, M.A.; Batool, S.S.; Farooq, M.; Shah Bukhari, S.N.U.; Chandio, A.D.; et al. Effective Removal of Methylene Blue by Mn_3O_4/NiO Nanocomposite under Visible Light. *Separations* **2023**, *10*, 200. <https://doi.org/10.3390/separations10030200>

Academic Editors: Yunqiao Zhou, Sheng Zhang, Bin Shi and Yueqing Zhang

Received: 30 January 2023
Revised: 3 March 2023
Accepted: 6 March 2023
Published: 14 March 2023



Copyright: © 2023 by the authors. Licensee MDPI, Basel, Switzerland. This article is an open access article distributed under the terms and conditions of the Creative Commons Attribution (CC BY) license (<https://creativecommons.org/licenses/by/4.0/>).

Abstract: Wastewater treatment is indispensable as wastewater can lead to adverse health effects and deteriorate the quality of life on earth. Photocatalysis is a facile methodology to address this issue. In this study, nanocomposites (NCs) of manganese oxide (Mn_3O_4) and nickel oxide (NiO) were synthesized in different weight ratios via the solid-state reaction route. Structural properties, optical properties, surface morphology, and functional group analysis of the synthesized nanomaterials were conducted using X-ray diffraction (XRD), UV–Vis spectroscopy, scanning electron microscopy (SEM) along with energy-dispersive X-ray (EDX) analysis, and Fourier-transform infrared (FTIR) spectroscopy, respectively. The bandgap of the nanocomposite decreases significantly from 2.35 eV for the Mn_3O_4 NPs to 1.65 eV for the Mn_3O_4/NiO nanocomposite (NC). Moreover, adsorption studies followed by the photocatalytic performance of the Mn_3O_4/NiO NCs were evaluated to determine the removal of methylene blue (MB) dye from wastewater. The photocatalytic performance of the nanocomposite enhances as the ratio of Mn_3O_4 in the composite increases from one weight percentage to three weight percentage. The photocatalytic degradation efficiency was calculated to be 95%. The results show that the synthesized NCs could play an important role in photocatalytic wastewater purification and environmental remediation.

Keywords: manganese oxide; nickel oxide; methylene blue; nanocomposites; photocatalysis; adsorption

1. Introduction

Water is vital for life, and its availability in its purest form is crucial to healthy life expectancy on earth. Water pollution, in comparison to other forms of pollution, poses a major

threat to living beings since effluents from various dye factories and tanneries contaminate water bodies [1]. The world's current primary challenge is the unavailability of safe drinking water [2]. An estimation of worldwide population regarding the unavailability of safe drinking water is about 1.2 billion, while the estimation regarding the lack of water accessibility for basic sanitary purpose is approximately 2.6 billion [3]. Asia and Africa are home to the majority of people who face pure water scarcity [4]. Multiple factors contribute to the contamination of clean water at a larger scale, such as climate change, population increase, soil degradation, inadequate sanitation, toxic algae, cleaning products, synthetic fertilizers, insecticides, pesticides, pharmaceuticals, pigment production, personal care products, disinfection byproducts, textile, leather, and dyeing [5–7]. According to recent studies, almost 15% of total dyes used in the textile industry remain unreacted, contributing significantly to effluents [1]. Various industries produce pollutants that contaminate water bodies. Statistically, the textile industry produces around 10 tons of fabric daily. Its water consumption is approximately 18 tons per day, while 4 million liters of water is produced as run off. Dye runoffs are hazardous as they contain organic and inorganic salts, acids, alkalis, and heavy metals that are poisonous, neurotoxic, teratogenic, and carcinogenic [5]. Among the various pollutants, some major ones that have gained substantial concerns owing to their serious threats to human health are fluorides, uranium, lead, copper, zinc, iodine, polymers, and a variety of organic pollutants [6]. Their prevalence has a harmful effect on living beings, including humans and animals, resulting in organ damage, skin rashes, nausea, vomiting, gastrointestinal tract irritation, and other problems [7]. Consequently, resolving this issue can improve not only human living conditions but also aquatic life.

Due to a growing concern about the safe removal of water pollutants, a number of advanced water treatment techniques have recently been used. For example, J. Jjagwe et al. worked on the synthesis and application of granular activated carbon from biomass waste materials for water treatment [8]. Granular activated carbon is presently used as a water treatment material to efficiently remove a variety of pollutants, including organic micropollutants, pharmaceuticals, arsenic and carcinogenic compounds, microplastics, heavy metals, as well as color and odor from pollutants [9]. Similarly, G. Gallareta-Olivares et al. used metal-doped carbon dots as robust nanomaterials for the monitoring and degradation of water pollutants [10]. Likewise, S. Jiang et al. used magnetically separable electrospun La-Mn-Fe tri-metal oxide nanofibers as a novel adsorbent for fluoride remediation [11]. Furthermore, J. Wang et al. worked on poly(amidoxime)-modified MOF macroporous membrane for high-efficient uranium extraction from seawater [12]. G. Zhou et al. fabricated Fir sawdust as a low-cost and easily recyclable adsorbent for the efficient removal of Pb (II), Cu (II), and Zn (II) [13]. Additionally, G. Obey et al. prepared biochar derived from non-customized matamba fruit shell as an adsorbent for iodine [2]. Moreover, S. Liu et al. prepared covalent organic frameworks [14] and J. Wang et al. prepared metal-organic framework materials (MOFs) for efficient water treatment with a super-high dye adsorption capacity at a high dye concentration [12].

Amongst the various treatment methods, photocatalysis is a highly attractive technique for the removal of dye pollutants due to its efficient capturing and transporting of light energy, use of visible light, and enhanced charge separation [15–18]. In this process, a photocatalyst is exposed to light, and if the light has sufficient energy, an electron–hole pair is generated. After the activation of the catalyst, oxygen is reduced, and organic compound is oxidized [19]. The reactant mass transfers to the surface of the photocatalyst, and then adsorption of the reactant occurs on the surface. Photocatalytic reaction takes place in an adsorbed state. The photogenerated charge carriers then move to the catalyst's surface. The activated catalyst absorbs photon energy equal or greater than the band gap, which transfers an electron from the valence band to the conduction band [20]. Hence, metal oxide semiconductors are extensively used in the process of photocatalysis [21].

Oxide-based semiconductors, such as ZnO, SnO₂, and TiO₂ MnO₂ [22–25], have played a central role in enhanced photodegradation process occurring at an accelerated rate [26]. However, their efficiency of degradation is still found to be limited. Therefore, the use of

co-catalysts is highly needed [27]. There is a vast range of applications of Mn_3O_4 NPs in various domains, including rechargeable batteries, ion-sieves, chemical sensing devices, catalysts, microelectronics, as well as optoelectronics [28]. Furthermore, Mn_3O_4 NPs have been reported as an effective photocatalyst for dye degradation [29,30]. NiO has been used as a co-catalyst to enhance the photocatalytic activity of some other metal oxides [31]. Due to the limitations in the photocatalytic performance of pure Mn_3O_4 NPs, NiO could be used as a co-catalyst to enhance the photocatalytic activity. The p-type semiconductor, NiO, has a significant photocatalytic role because of its larger gap between the conduction and valence bands [32]. NiO NPs have received significant attention because of some particular features, such as a bandgap of 3.6 eV, phase stability, increased magnetic permeability, and electrical conductivity [33]. These features are responsible for NiO NPs being considered ideal for photocatalysis [34]. Only a few reports are available about the synthesis of Mn_3O_4 /NiO nanocomposite for catalytic degradation. Therefore, the present work focuses on the fabrication of an efficient photocatalyst comprising Mn_3O_4 NPs in conjunction with NiO NPs to form a nanocomposite that can enhance photocatalytic performance and, thus, the removal of pollutants. To the best of our knowledge, the photocatalytic performance of Mn_3O_4 in conjunction with NiO NPs has not yet been reported in the literature. However, the photodegradation of Mn_3O_4 and NiO by itself and other nanocomposites, such as V/ Mn_3O_4 , Pb/ Mn_3O_4 , Ag/ Mn_3O_4 , Fe/NiO and Mn_3O_4/γ -MnOOH etc., (mentioned in Table 2) have been studied before [35–46].

2. Experimental

2.1. Materials

The reagent-grade chemicals used in this study included extra pure manganese chloride tetrahydrate ($MnCl_2 \cdot 4H_2O$), with a molecular weight of 197.91 g/mol; nickel chloride hexahydrate ($NiCl_2 \cdot 6H_2O$), with a molecular weight of 129.59 g/mol and 98% purity; cetyl tetra butyl ammonium bromide (CTAB), with a molecular weight of 322.37 g/mol and 98% purity; and sodium hydroxide (NaOH). All chemicals were purchased from Sigma Aldrich, Germany. Double distilled (DD) water was used to prepare the molar solutions of these chemicals.

2.2. Synthesis of Pure Mn_3O_4 Nanoparticles

A simple chemical precipitation method was used to synthesize Mn_3O_4 NPs at room temperature. A calculated amount of NaOH (0.88 g) was dissolved in 100 mL of distilled water at room temperature for almost ten minutes. To this solution, 2.177 g of $MnCl_2 \cdot 4H_2O$ was dissolved with continuous stirring. To suppress the reunion of nanoparticles, 25 mg of cetyl tetra methyl ammonium bromide (CTAB) was added as a surfactant with constant stirring. After 24 h of stirring, a brown-colored precipitate was formed, which indicated the completion of reaction. The resulting precipitate was then filtered, followed by washing with DD water several times and drying overnight in a hot air oven at roughly 80 °C. Next, thermal treatment of the as-prepared sample was performed at 500 °C for 2 h under air at a ramping rate of 5 °C min^{-1} to remove the surfactant CTAB. As a result of calcination, the brown color of the sample was turned into black. In the Supplementary Materials, Figure S1a–f show the different steps of the preparation of Mn_3O_4 NPs in the laboratory.

2.3. Synthesis of Pure NiO Nanoparticles

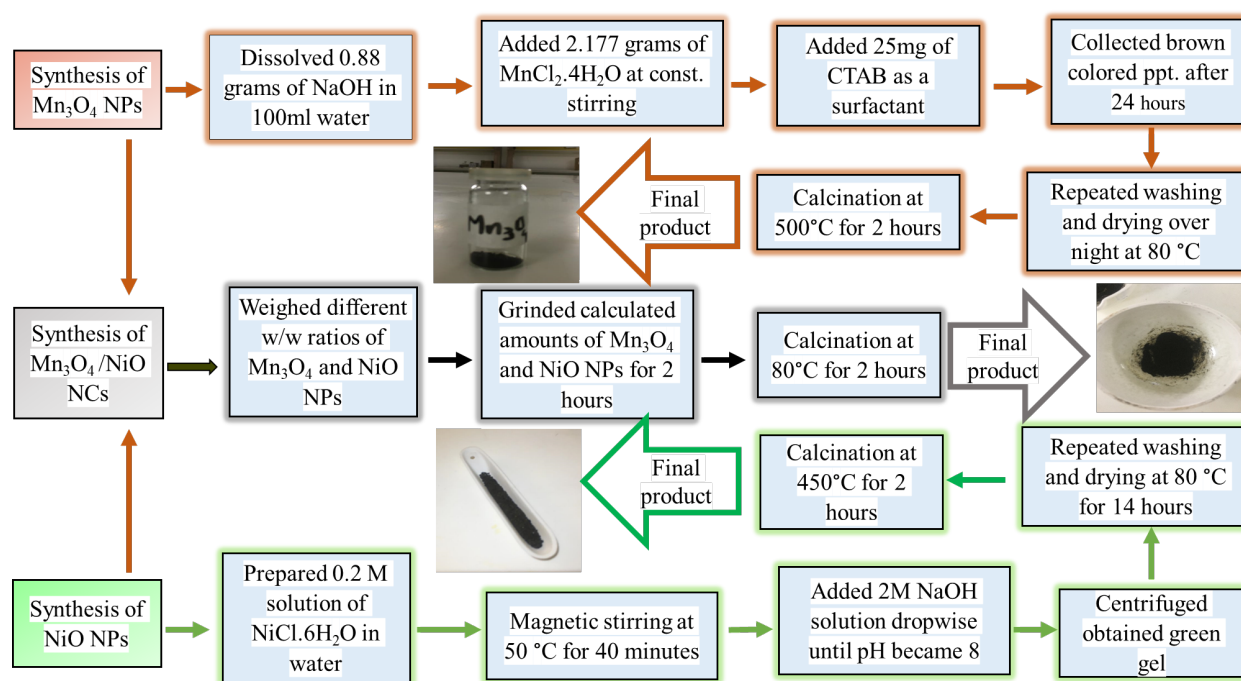
Nickel oxide NPs were synthesized by a simple co-precipitation method. At first, a 0.2 M of nickel chloride hexahydrate solution was prepared in deionized water and magnetically stirred for 40 min at 50 °C. A total of 2 M of NaOH solution was prepared in DI water and added to the above-mentioned solution dropwise at room temperature until the pH became 8. The produced green gel was subjected to centrifugation, and the extracted gel was then rinsed with DD water and ethanol. The gel was dried under vacuum at 60 °C for almost 14 h. The formed nickel hydroxide was subjected to calcination for 2 h at 450 °C in a tube furnace in order to obtain NiO NPs. The sample's color changed from

green to greyish black as a result of the annealing process. Figure S2a–d show the different steps of the preparation of NiO NPs in the laboratory. The following equation shows the overall chemical reaction to synthesize NiO NPs:



2.4. Synthesis of $\text{Mn}_3\text{O}_4/\text{NiO}$ Nanocomposites

The prepared Mn_3O_4 and NiO NPs were used to synthesize $\text{Mn}_3\text{O}_4/\text{NiO}$ NCs in different *w/w* ratios by using a simple solid-state method. In order to synthesize $\text{Mn}_3\text{O}_4/\text{NiO}$ NC at a ratio of (1:1), equally weighted amounts of Mn_3O_4 and NiO NPs were grounded for almost one hour, followed by calcination at about 80 °C for two hours in a tube furnace. The temperature of 80 °C was used to adhere the two materials through Van der Waal forces, and the successful formation of the physically prepared composite system was used for an evaluation of the photocatalytic properties of the two different materials together in single physical phase. $\text{Mn}_3\text{O}_4/\text{NiO}$ NC at a ratio of (3:1) was synthesized by taking 3 times the amount of Mn_3O_4 to the amount of NiO NPs to make a composite with a 3:1 concentration, following the same procedure mentioned before. The different steps of the preparation of the $\text{Mn}_3\text{O}_4/\text{NiO}$ nanocomposites in the laboratory are shown in Figure S3a–c. An overview of the whole experimental process is shown in the following schematic illustration (Scheme 1).



Scheme 1. Schematic illustration of the experimental process for the synthesis of Mn_3O_4 NPs, NiO NPs, and $\text{Mn}_3\text{O}_4/\text{NiO}$ NCs.

2.5. Evaluation of Adsorption and Photocatalytic Activity of $\text{Mn}_3\text{O}_4/\text{NiO}$ Nanocomposites

The photocatalysis of the nanocomposites of Mn_3O_4 and NiO was performed by taking methylene blue as a model pollutant. Methylene blue ($\text{C}_{16}\text{H}_{18}\text{ClN}_3\text{S}$) is a potentially hazardous organic cationic dye that is water soluble. The photocatalytic experiment was performed under direct sunlight.

Before studying the photocatalytic activity, an adsorption/batch study was performed in the dark (without light). A stock solution of 998.86 mg/L was first prepared, and, from this solution, further dilute solutions of different mg/L (2, 4, 6, 8, and 10) were obtained. After an analysis of the data from the calibration curve, a batch study was performed in the dark at a concentration of 5.99 mg/L. For the adsorption experiment, the pH of the

sample was kept at 7, and the experiment was performed at a concentration of 998.86 mg/L. Various solutions at 10 mL were obtained from this solution. A total of 10 mg of the catalyst was added in all the solutions, and then they were kept for agitation in a shaker bath at different times. After agitation, the samples were centrifuged, filtered, and then examined under UV–Vis spectroscopy.

After the batch study, the next experiment was a pH study which was also performed in the dark. In the pH study, 499.43 mg/L of the stock solution was prepared in 250 mL of deionized water. The same steps were followed as explained earlier in the adsorption study; however, different solutions of 10 mL were prepared at different pH values, i.e., 2, 7 and 11, by using acidic and basic buffer solutions, such as 0.1 M acetate buffer and 0.1 M ammonium hydroxide and ammonium chloride buffer solution, respectively.

The photocatalytic performance of the nanocomposites was investigated by using the organic dye, methylene blue, under natural visible light illumination. The synthesized nanocomposites with different ratios (1:1, 2:1, and 3:1) were transferred into 50 mL of 799.62 mg/L and 399.81 mg/L of MB dye solution. The degradation experiment was accomplished after achieving an adsorption/desorption equilibrium state of the MB dye on the surface of the catalyst. The mixture was then exposed to direct sunlight at different time intervals of 50–350 min. At the end, the degradation of the MB dye was assessed by carefully measuring the residual concentration of the MB dye from the vial with the help of a UV–Visible spectrophotometer. The dye removal percentages for the synthesized nanocomposites were calculated using the following formula:

$$\text{Dye removal \%} = \frac{C_0 - C_t}{C_0} \times 100 \quad (2)$$

where ' C_0 ' and ' C_t ' are the MB dye absorbance before degradation and final absorbance of the dye at regular time intervals ' t ' under natural light irradiation, respectively.

2.6. Characterization

The X-ray diffraction (XRD) analysis of the synthesized samples was performed with the help of a (STOE, Darmstadt, Germany) Theta-Theta S/N 65022 diffractometer with $\text{CuK}\alpha$ radiation. A (JEOL, Akishima, Japan) JSM-6490A electron scanning microscope (SEM) equipped with an energy-dispersive spectroscopy (EDS) was used for the morphological, microstructural, and elemental analyses. The optical analysis of the sample material was performed by using an OPTIZEN Alpha UV/Vis Spectrophotometer (Shang hai, China). For the functional group analysis, a (Perkin Elmer, Waltham, MA, USA) Spectrum 100 Fourier-transform infrared spectrophotometer (FTIR) was employed.

3. Results and Discussion

3.1. Structural Analysis of the Synthesized $\text{Mn}_3\text{O}_4/\text{NiO}$ NPs and NCs

The XRD spectra for the pure Mn_3O_4 and NiO NPs and NCs are shown in Figure 1. The pure Mn_3O_4 NPs show diffraction peaks located at the Bragg angles (2θ) \cong 38.48, 44.61, 64.83, 72.61, and 78.06 parallel to the crystal planes (004), (220), (400), (332), and (325), respectively; these results precisely resemble the values reported by the Joint committee on Powder Diffraction Standards (JCPDS card no. 01-080-0382). The structure formed is highly crystalline and has a tetragonal shape. By using the Debye–Sherrer formula, the average crystallite size was calculated to be 24.94 nm, and the average lattice strain (ϵ) was found to be 0.0033 [38]. The FWHM and d-spacing values, along with the (hkl) and 2θ degrees, are listed in the Supplementary Materials in Table S1. The pure NiO NPs show various diffraction peaks located at the Bragg angles (2θ) \cong 36.6°, 42.7°, 44.6°, 62.5°, and 72.7° parallel to the crystal planes (003), (012), (200), (104), and (311), respectively; these results also precisely resemble the values reported by the Joint Committee on Powder Diffraction Standards (JCPDS card no. 00-022-1189 and 00-047-1049). The average crystallite size was calculated to be 21.51 nm, and the average lattice strain (ϵ) was found to be 0.0054 [39]. The values for the FWHM and d-spacing values are shown in Table S2.

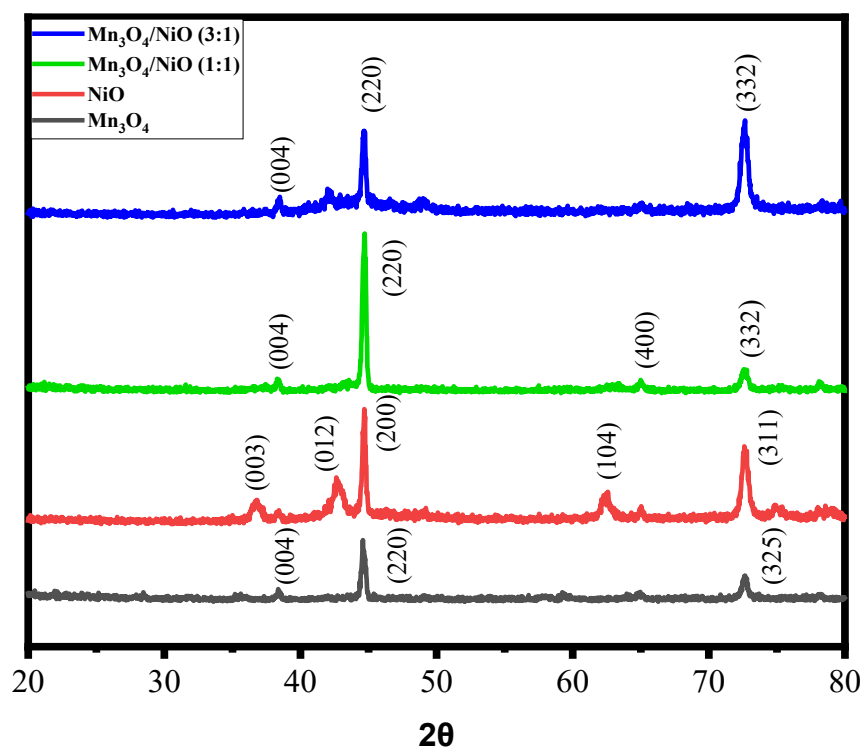


Figure 1. XRD spectra of the Mn_3O_4 NPs, the NiO NPs, and the $\text{Mn}_3\text{O}_4/\text{NiO}$ NCs in different ratios.

The nanocomposite $\text{Mn}_3\text{O}_4/\text{NiO}$ (1:1), as revealed in Figure 1, shows diffraction peaks located at the Bragg angles (2θ) \cong 38.31°, 44.71°, 64.98°, 72.63°, and 78.08° parallel to the crystal planes (004), (220), (400), (332), and (325), respectively, which precisely resemble the values reported by the Joint Committee on Powder Diffraction Standards (JCPDS card no. 01-080-0382 and 00-022-1189). By using the Debye–Sherrer formula, the average crystallite size was calculated to be 30.87 nm, and the average lattice strain (ϵ) was found to be 0.0026. The FWHM values are shown in Table S3. The nanocomposite $\text{Mn}_3\text{O}_4/\text{NiO}$ (3:1) shows diffraction peaks located at the Bragg angles (2θ) \cong 38.48°, 42.11°, 44.71°, 72.63°, and 78.23° parallel to the crystal planes (004), (012), (220), (332), and (325), respectively, which also precisely resemble the values reported by the Joint Committee on Powder Diffraction Standards (JCPDS card no. 01-080-0382 and 00-022-1189). Only a small shift in the peak positions distinguishes the diffraction patterns of the pure and modified Mn_3O_4 with NiO NPs, and the intensity of the pure sample is lower than that of the modified sample. A little shift toward the left indicates the NiO doping in manganese oxide. The average crystallite size was calculated to be 25.93 nm, and the average lattice strain (ϵ) was found to be 0.00372 for the NC 3:1. The structure formed is highly crystalline in nature. The values for FWHM and d-spacing are listed in Table S4.

3.2. Morphological and Elemental Analyses of $\text{Mn}_3\text{O}_4/\text{NiO}$ NPs and NCs

The morphological characterization of the synthesized nanoparticles and their composites were performed using scanning electron microscopy along with energy-dispersive X-ray analysis. Figure 2 shows the morphology of the Mn_3O_4 and NiO NPs and the $\text{Mn}_3\text{O}_4/\text{NiO}$ NCs (1:1 and 3:1). Spherical aggregated nanoparticles of Mn_3O_4 with diameters ranging from 20 to 80 nm are observed, as revealed in Figure 2a. Figure 3a–d show the EDX spectra of the Mn_3O_4 and NiO NPs and the $\text{Mn}_3\text{O}_4/\text{NiO}$ NCs 1:1 and 3:1, respectively. The peaks corresponding to manganese, nickel, and oxygen are present in the spectra, which further confirms the successful synthesis of the targeted Mn_3O_4 and NiO NPs and NCs. An unknown peak is also observed in the EDX spectra of the Mn_3O_4 and NiO NPs, which is suspected to be from the solvent used. The atomic and weight percentage for each element are presented in Table 1. The SEM image of the synthesized NiO nanoparticles at

450 °C is shown in Figure 2b. The SEM image clearly indicates smaller, spherical grains with diameters ranging from 35 to 60 nm. The SEM image of the nanocomposite of Mn₃O₄ and NiO 1:1 (one part NiO and one part Mn₃O₄) is shown in Figure 2c, whereas Figure 2d shows the SEM image of the composite 3:1 (three parts Mn₃O₄ and one part NiO). The particles exhibit a spherical shape and have a non-uniform size distribution because of agglomeration. The pure Mn₃O₄ has a smooth surface, but clusters are developed with NiO doping and, hence, the grain size has increased, which is also in accordance with the XRD results. The weight percentages of manganese and oxygen in the pure sample are 80.9% and 19.1%, respectively, whereas in the NiO-modified sample, the weight percentage varies according to the doping concentration, as shown in Table 1 [36,40].

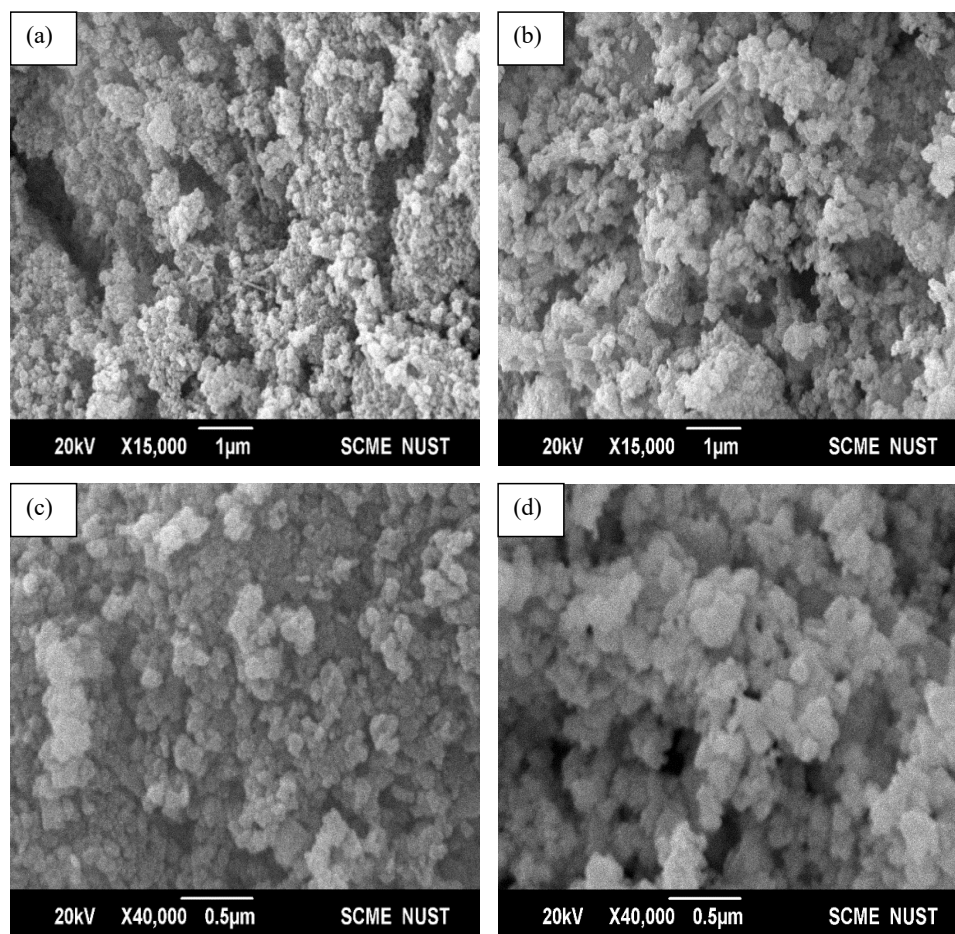


Figure 2. SEM images of (a) Mn₃O₄ NPs, (b) NiO NPs, (c) 1:1 Mn₃O₄/NiO NC, and (d) 3:1 Mn₃O₄/NiO NC.

3.3. Optical Analysis of Mn₃O₄/NiO NPs and NC

The UV–Vis spectrum of the Mn₃O₄ NPs synthesized with the precursor manganese chloride tetrahydrate is shown in Figure 4a. The characteristic peak in the UV–Vis spectrum at 240 nm exhibits a remarkable agreement with the values reported in the literature for Mn₃O₄ nanoparticles [47]. The band gap energy of the synthesized NPs and NCs were calculated using the Tauc’s equation as given below:

$$(\alpha h\nu)^n = A(h\nu - E_g) \tag{3}$$

where ‘A’ is a constant; ‘E_g’ is the band gap of the material; ‘α’ is the absorption coefficient; ‘h’ is the incident photon energy; and ‘n’ is the exponent that depends on the kinds of

transition. For direct or allowed transition, it is a value of $n = 2$, and for indirect transition, it is value of $n = 1/2$. It can also be expressed as follows:

$$E_g = hc/\lambda \tag{4}$$

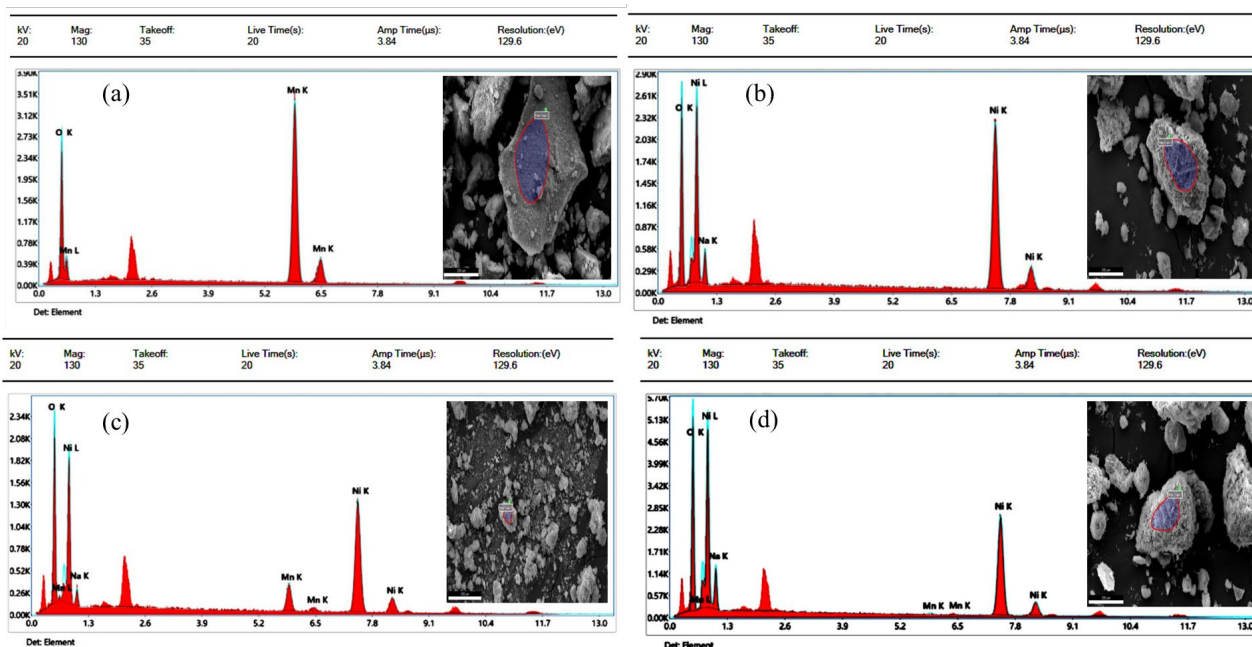


Figure 3. (a) EDX image of pure Mn_3O_4 NPs, (b) EDX image of pure NiO NPs, (c) EDX image of Mn_3O_4/NiO NC (1:1), and (d) EDX image of Mn_3O_4/NiO NC (3:1).

Table 1. Weight and atomic % of the Mn_3O_4 NPs, the NiO NPs, and the Mn_3O_4/NiO (1:1) and (3:1) NCs.

Materials	Element	Weight %	Atomic %
Mn_3O_4 NPs	O K	19.1	44.7
	Mn K	80.9	55.3
NiO NPs	O K	23.1	46.0
	Na K	14.5	20.1
	Ni K	62.5	33.9
Mn_3O_4/NiO NC 1:1	O K	22.5	48.3
	Na K	5.2	7.8
	Mn K	37.5	23.5
	Ni K	34.8	20.4
Mn_3O_4/NiO NC 3:1	O K	27.6	50.7
	Na K	16.6	21.2
	Mn K	39.1	21.5
	Ni K	16.7	6.6

To calculate the direct band gap of the sample material, a graph is plotted between $h\nu(eV)$ and $(\alpha h\nu)^2(eVcm^{-1})^2$, which is shown in the inset of Figure 4a. For the Mn_3O_4 NPs, the bandgap energy was calculated to be 2.35 eV. The UV–Vis absorption spectrum of the NiO NPs is shown in Figure 4b. An absorption peak is discovered in the electromagnetic area of ultraviolet light. The characteristic peak at 230 nm in the UV–Vis spectrum clearly indicates the synthesis of NiO NPs, and the bandgap energy was calculated to be 3.15 eV [48]. The UV–Visible spectrum of the Mn_3O_4/NiO NC is shown in Figure 4c. Absorption peaks are discovered in the electromagnetic area of ultraviolet light. The characteristic peaks at

230 nm and 370 nm are observed in the UV-Vis spectrum of the Mn₃O₄/NiO nanocomposite, where a red shift can be observed (a shift toward longer wavelength). This red shift is attributed to the lattice distortion and new localized bands being introduced. On the host matrix, an increase in dopant concentration is the reason that causes the formation of these localized bands. However, the bandgap energy calculated by the Tauc plot was found to be 1.65 eV for Mn₃O₄/NiO, as shown in the inset of Figure 4c.

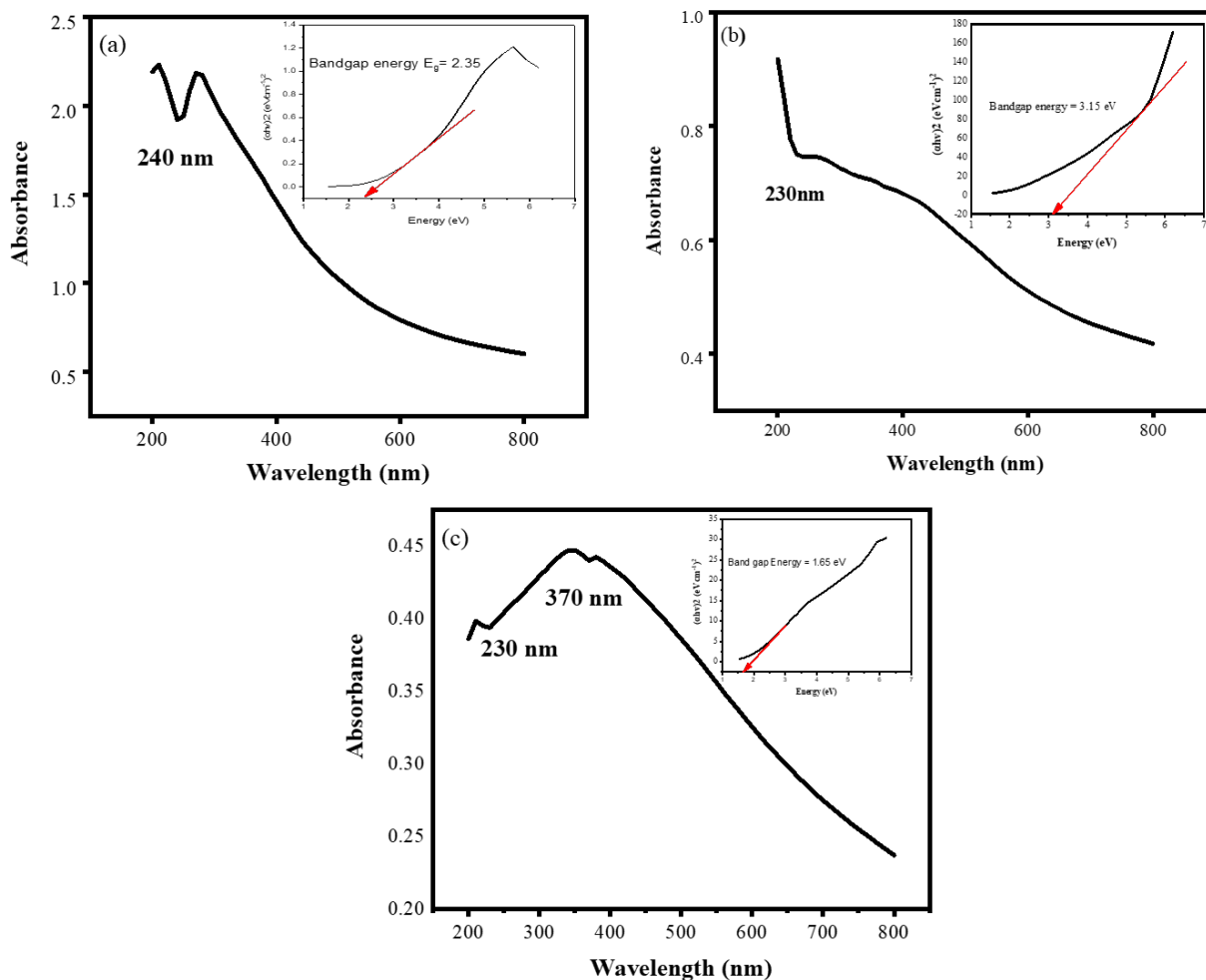


Figure 4. UV-Vis spectra of (a) Mn₃O₄ NPs, (b) NiO NPs, and (c) Mn₃O₄/NiO NC 1:1 with bandgap energy.

3.4. Functional Group Analysis of Mn₃O₄/NiO NPs and NCs

The FTIR spectra of the synthesized Mn₃O₄ and NiO NPs and the Mn₃O₄/NiO NCs are shown in Figure 5. From the corresponding spectra obtained in the wavelength range from 4000 to 400 cm⁻¹, the presence of functional groups and bonds can be inferred. In Figure 5, the black colored plot represents the Mn₃O₄ spectrum, where the peak at 3421 cm⁻¹ shows the stretching vibration of OH group while the peak at 1632 cm⁻¹ shows the absorption of moisture on the sample surface. The peak at 1020 cm⁻¹ shows the bending vibrations of Mn atoms with -OH groups. The bands at 623 cm⁻¹ and 482 cm⁻¹ indicate the stretching modes of the tetrahedral and octahedral sites in Mn-O [49].

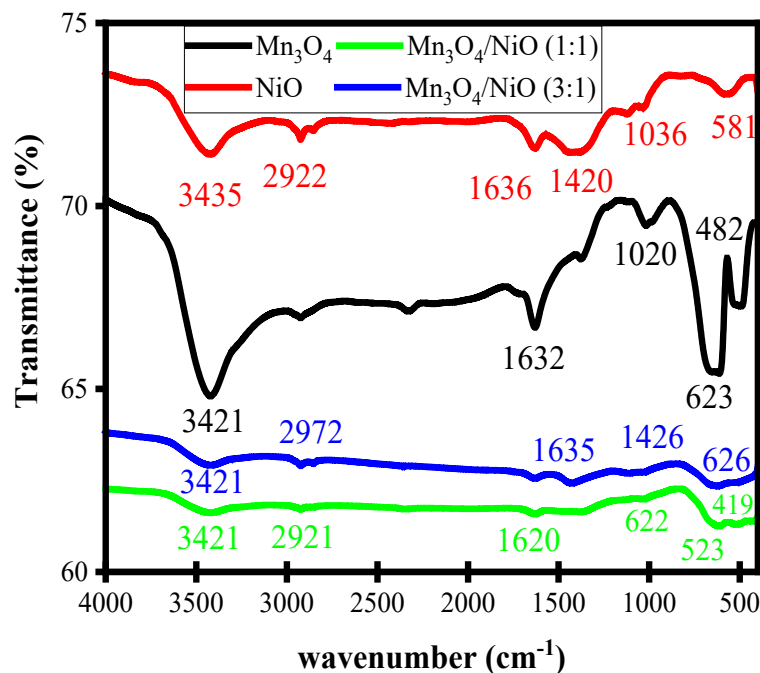


Figure 5. FTIR spectra of pure Mn_3O_4 NPs, NiO NPs, and $\text{Mn}_3\text{O}_4/\text{NiO}$ NCs (1:1) and (3:1).

Red color represents the FTIR spectrum of the NiO nanoparticles calcined at $450\text{ }^\circ\text{C}$ for two hours. The broad bands, as previously described, correspond to O-H stretching due to the presence of adsorbed water from the atmosphere on the surface of the NiO nanoparticles, whereas the adsorption band in the region of 581 cm^{-1} corresponds to NiO-stretching vibrations [32].

Figure 5 also shows the FTIR spectra of the 1:1 and 3:1 $\text{Mn}_3\text{O}_4/\text{NiO}$ nanocomposites in green and blue color, respectively. In both spectra, the band at 3421 cm^{-1} shows the stretching vibration of OH group, while the peak in the region of 1600 cm^{-1} shows the absorption of moisture on the sample surface. The bands at 1021 cm^{-1} and 1016 cm^{-1} in the nanocomposites with a 1:1 and 3:1 ratio show bending vibrations of Mn atoms with $-\text{OH}$ groups. The bands in the region of 600 cm^{-1} , 500 cm^{-1} , and 400 cm^{-1} indicate the stretching modes of Mn-O and Ni-O. Noticeably, the characteristic peak at 623 cm^{-1} for the Mn_3O_4 NPs is observed in the nanocomposites, which further proves the successful synthesis of the $\text{Mn}_3\text{O}_4/\text{NiO}$ NCs.

3.5. Adsorption Study of MB Dye Using $\text{Mn}_3\text{O}_4/\text{NiO}$ NCs

Without adding any catalyst, a maximum absorption peak is obtained at 660 nm with a full scan of the adsorption of MB dye for comparison. Figure S4 shows the calibration curve for the stock sample solution. For the adsorption experiment, the pH of the sample was optimized at 7, and the experiment was performed at a concentration of 6 ppm. Figure 6a shows the experimental data of the adsorption of MB dye against contact time for the Mn_3O_4 -based nanomaterial. Figure 6b shows the kinetic study of the adsorption process in the dark. It indicates that the adsorption of MB dye increases linearly with increase in time interval with a fixed adsorbent amount (10 mg) and becomes slow after 60 min. After nearly 80 min of the adsorption experiment, saturation occurs. Initially, the kinetic rate is very high, and as time increases, it becomes slow until it attains equilibrium. Initially, the Mn_3O_4 NPs have a large number of unoccupied active sites, which decreases after a transition of time. The decrease in the absorbance peak in Figure S5 clearly indicates the adsorption phenomenon. The main aim of conducting the adsorption study was to confirm whether efficient dye removal could be made possible by using the adsorption phenomenon only. However, the results from the adsorption study are not very satisfactory, which suggests a need to opt for photocatalytic activity for efficient dye removal. In order

to make the test fair, the adsorption phenomenon was tested further at different pH values (as described in the next section). Here, the results again support the fact that light has a major role in the activation of the catalyst. This evidence supports testing for photocatalytic activity for efficient dye removal.

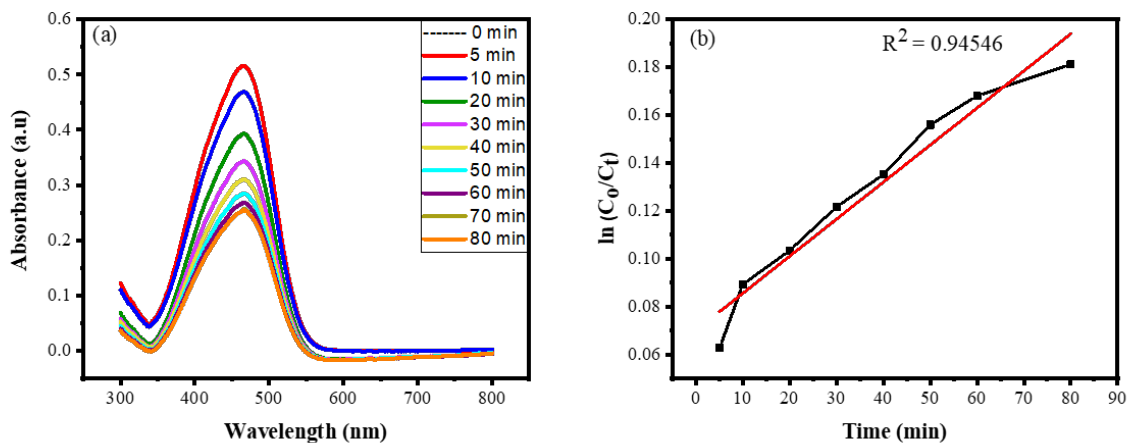


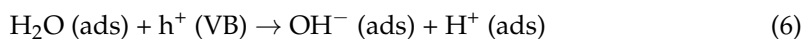
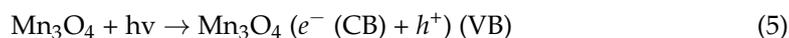
Figure 6. (a) Adsorption of MB dye in the presence of Mn₃O₄-based nanomaterials, and (b) kinetic study of the adsorption process in the dark.

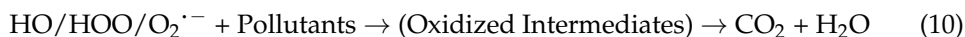
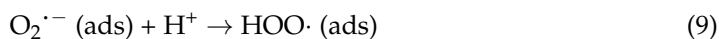
3.6. Effect of pH on Adsorption of MB Dye

The chemical properties of both the MB dye and the adsorbent (Mn₃O₄) generally change with the pH of the adsorbate solution MB. Thus, it is important to study the pH effect on the adsorption of MB by the Mn₃O₄ NCs. The experiment performed for the pH study was also performed in the dark, and the same steps were followed as explained earlier in the adsorption study; the only difference was that those different 10 mL solutions were optimized at different pH, i.e., 2, 7, and 11. Figure 7a–c show the adsorption of MB dye by using the Mn₃O₄/NiO NCs as a catalyst at a pH of 2, 11, and 7, respectively. Figure 7b shown below indicates that the maximum value of adsorption for MB dye is at a pH of 11, which is a basic medium. The minimum adsorption occurs at a pH of 2, which is an acidic medium. Adsorption is very slow in the acidic medium and gradually increases as it moves toward the basic medium, but it still does not give satisfactory results in terms of considerable dye removal.

3.7. Photocatalysis under Visible Irradiation

When light is turned on, photocatalytic reaction begins. The valence band will be breached by the creation of an electron–hole pair because of the transition of electron from the valence band to the conduction band. This will lead to a photogenerated e[−]/h⁺ pair. This process occurs when light interacts with a material having a wavelength within the bandgap of the semiconductor. This light has an optical energy comparable to the semiconductor’s bandgap. Charge carriers can then travel from the bulk to the surface of the material. If dissolved oxygen is deposited on the photocatalyst’s surface in an aqueous solution, reduction will take place by electrons, resulting in superoxide radical anions, O₂^{•−}, whereas holes can oxidize both water and hydroxyl anions, resulting in hydroxyl radicals, HO•. Furthermore, O₂^{•−} can form hydroperoxyl radicals, HOO•, by protonation [34].





However, ‘scavenging’ reactions such as charge recombination might occur, thereby lowering the photocatalyst’s effectiveness.

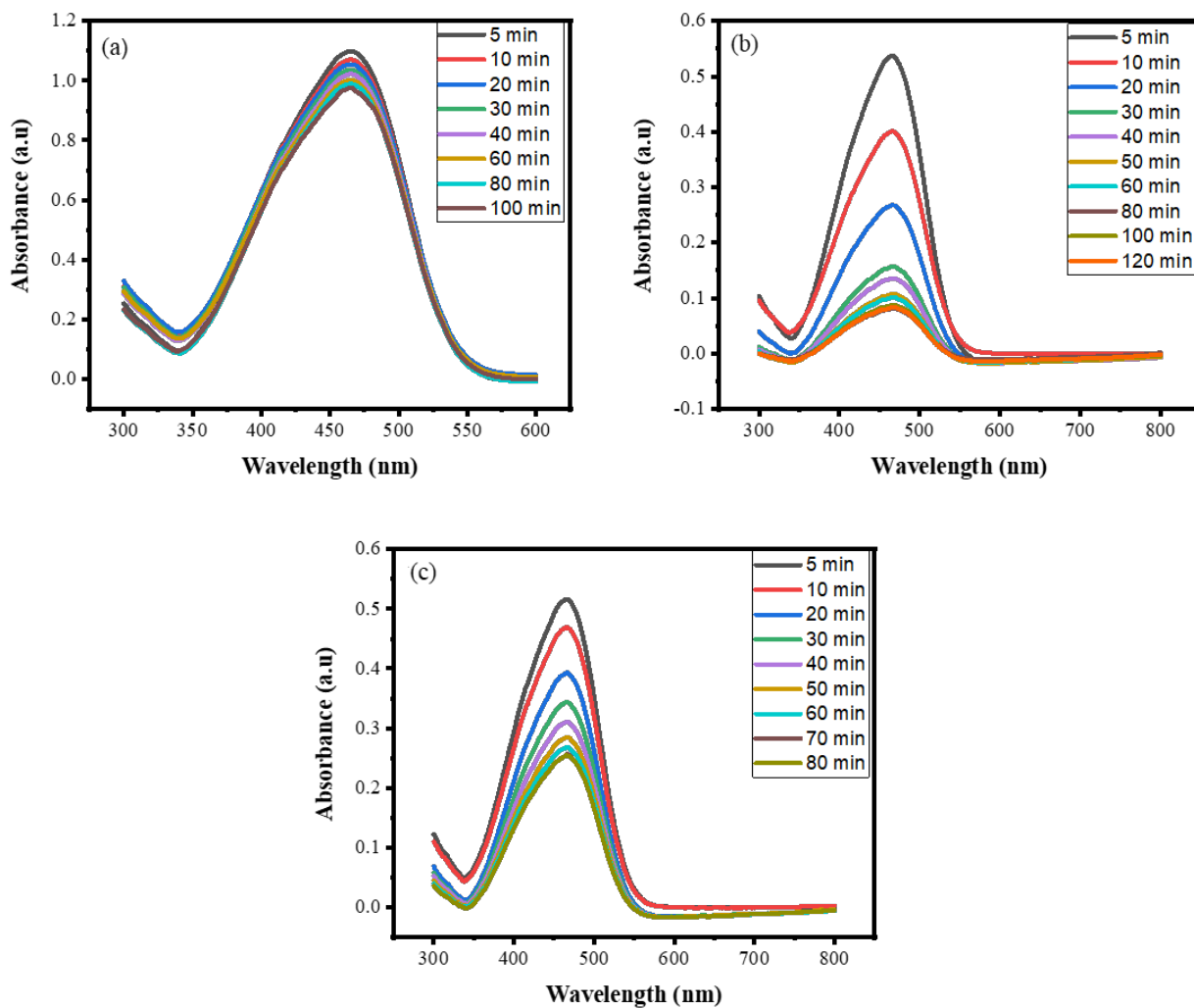


Figure 7. MB dye adsorption in the presence of the Mn₃O₄/NiO NC (a) at pH of 2, (b) at pH of 11, (c) at pH of 7.

For photocatalytic activity, the pH of the sample was optimized at seven. Figure 8a–c shows the UV–Vis absorbance curves with wavelength for different sample solutions of the Mn₃O₄/NiO nanocomposites. The maximum absorption peak is obtained at 657 nm with a full scan of the adsorption of MB dye. The graphs show how the absorbance intensity decreases with an increase in the irradiation time. The absorption intensity of MB dye drops progressively with an increase in irradiation time without a change in the wavelength of absorption. This shows that in the presence of the Mn₃O₄ photocatalyst, considerable dye removal occurs.

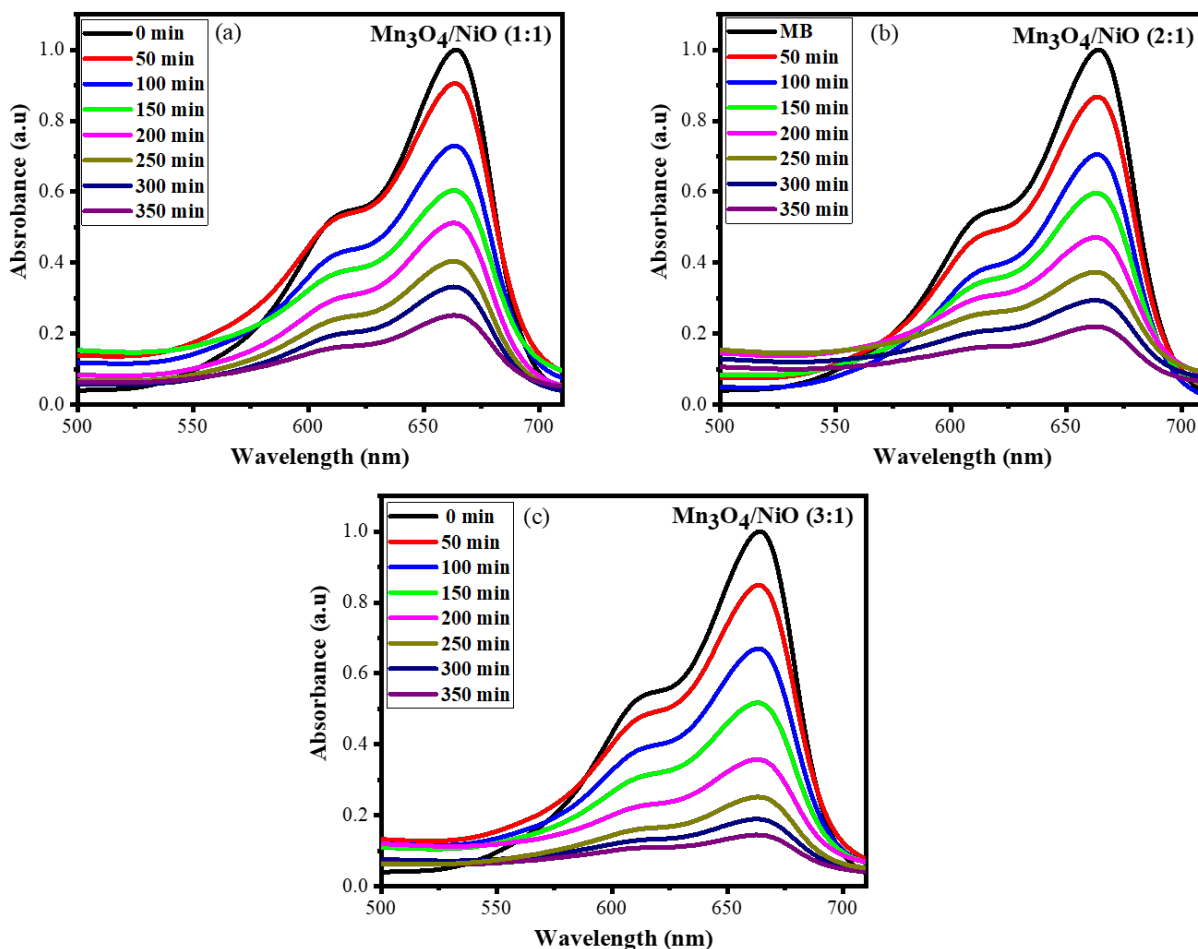


Figure 8. UV-Visible absorption spectra of the (a) NC Mn₃O₄/NiO (1:1), (b) NC Mn₃O₄/NiO (2:1), and (c) NC Mn₃O₄/NiO (3:1) under visible light at 657 nm.

Figure 9a shows the kinetic study of the photocatalytic process, which indicates that the adsorption of MB dye increases linearly with an increase in time interval. Initially, the kinetic rate is very high as the time increases. Figure S6 shows the remaining concentration of dye with respect to time. Initially, there is a large number of unoccupied active sites, which decreases with the transition of time, and thus, a descending curve is obtained here. After a definite time interval, the reaction attains an equilibrium state. Figure 9b shows the percentage of dye removal for the three composites at regular intervals. As obvious from the curves in the graphs, the Mn₃O₄/NiO (3:1) NC shows the best photocatalytic activity, with 95% dye removal efficiency, whereas the Mn₃O₄/NiO (1:1) NC shows 91% and the Mn₃O₄/NiO (2:1) NC shows 92% dye removal efficiency [50].

As shown in Figure 10, the pseudo-first order (PFO) kinetic model is most suited to understand the photocatalysis process and the reaction rate during the process, as provided by the following equation:

$$\ln \frac{C_0}{C_t} = k_{app}t \tag{14}$$

where ‘C₀’ is the initial dye concentration prior to illumination; ‘C_t’ is the concentration of the dye after each time interval *t*; and *k_{app}* is the apparent rate of the photocatalytic reaction. In Figure 10, ‘*q_e*’ and ‘*q_t*’ represent the amount of dye adsorbed at equilibrium and at any time ‘*t*’.

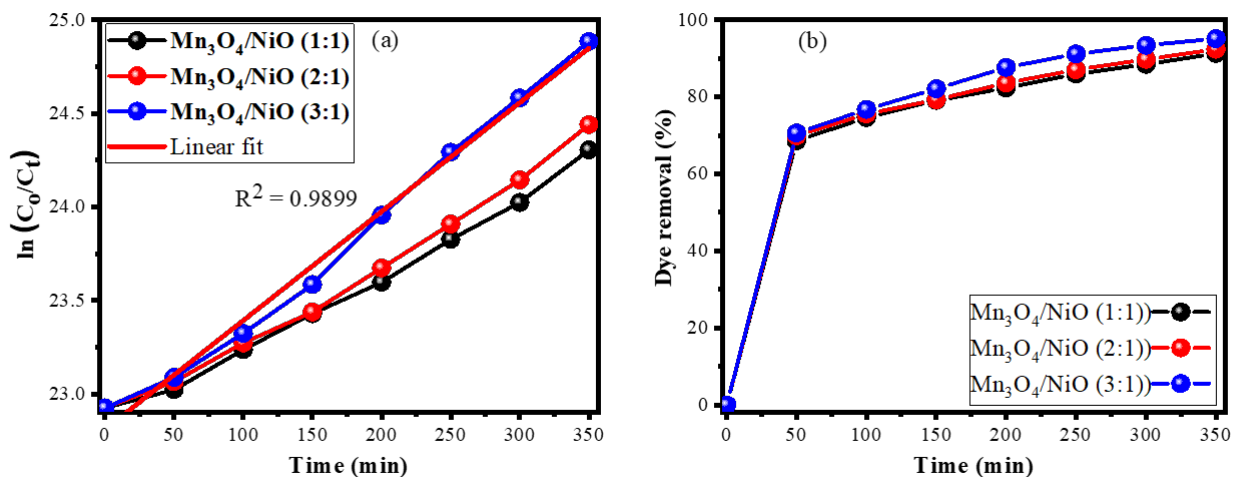


Figure 9. (a) Kinetic study of the photocatalytic process for the Mn₃O₄/NiO nanocomposites, and (b) dye removal percentage at different time intervals.

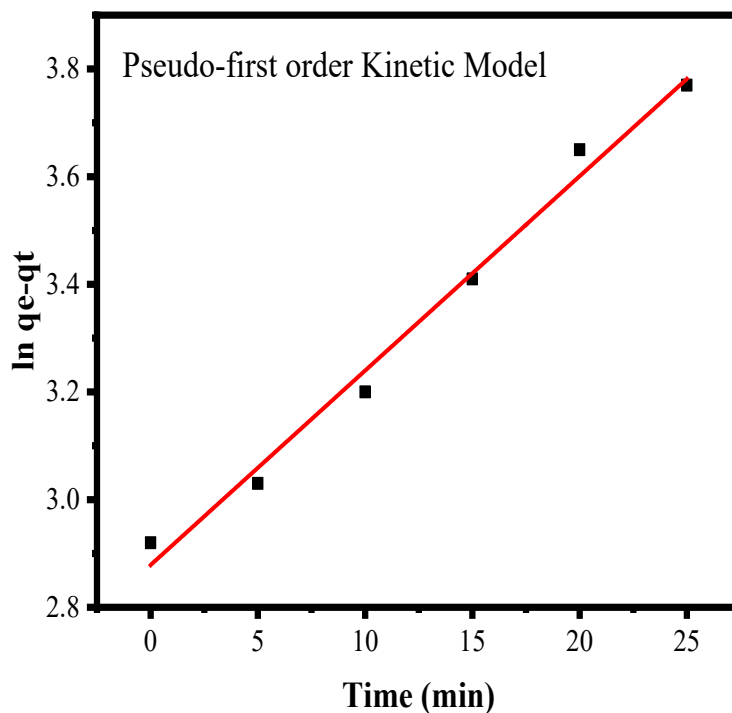


Figure 10. Pseudo-first order kinetic model for photocatalytic activity.

Using the equation for the pseudo-first order reaction, the value of the rate constant was calculated to be 0.0014 min^{-1} .

A comparative study of the photocatalytic degradation efficiency of the pure Mn₃O₄ NPs and Mn₃O₄/NiO NCs with different existing nanostructures is presented in Table 2. The pure Mn₃O₄ NPs have less degradation efficiency compared to the Mn₃O₄/NiO NCs [36]. It can be concluded that the Mn₃O₄/NiO NCs are a potential candidate for photodegradation of harmful pollutants in comparison to the sole Mn₃O₄ NPs and can also be used in other related environmental applications.

Table 2. Comparative study of the photodegradation efficiency of the proposed catalysts against reported photocatalysts in the literature.

Catalyst	Structure of Catalyst	Dye Degraded	Dye Removal Percent	Rate Constant (min ⁻¹)	References
Mn ₃ O ₄	Nanoparticles	Methylene blue	68% (UV)	0.003	[36]
Ag-TiO ₂	Nanoparticles	Methyl orange	72.48% (UV) 48.08 (Visible)	0.00395	[41]
Graphene/Ag/TiO ₂	Nanocomposite	Yellow 2	-	0.022	[42]
Ce/ZnO	Nanocomposite	Methylene blue	96%	0.007	[21]
Ag/ZnO	Nanoparticles	Chlorophenol	57% (UV)	-	[43]
Fe-NiO	Nanoparticles	Methylene blue	85% (UV)	0.031	[44]
Ag/Mn ₃ O ₄	Nanoparticles	Congo red	89% (UV + Visible)	-	[45]
Ag/Mn ₃ O ₄	Nanoparticles	Methylene blue	90% (Visible)	0.024	[20]
Mn ₃ O ₄ /γ-MnOOH	Nanocomposite	Norfloxacin	-	0.0720	[46]
Mn ₃ O ₄ /NiO	Nanocomposite	Methylene blue	95%	0.0014	Present

4. Conclusions

Manganese oxide (Mn₃O₄) and nickel oxide (NiO) NPs and their composites in three different ratios were synthesized using a solid-state reaction method. Using XRD, the successful and complete formation of Mn₃O₄ and NiO NPs at 450 °C was observed. The XRD data demonstrated that the material prepared at 450 °C had a larger crystallinity, which is why this sample was chosen for further processing. Using the Scherrer's formula, the average crystallite size was calculated to be about 0.152 nm for Mn₃O₄ and 0.168 nm for NiO. The FTIR data further demonstrated the presence of respective functional groups in the synthesized sample. The UV-Vis spectroscopy was used to investigate the absorption spectrum of the Mn₃O₄ and NiO NPs and NC in the wavelength range from 200 to 800 nm. The calculated bandgap of the synthesized sample from the Tauc plot was 2.35 eV for Mn₃O₄ and 3.15 eV for NiO, which are very close to the results reported in the literature. Since the results from the adsorption studies were not very satisfactory, photocatalytic activity was opted for efficient dye removal. Several photocatalytic treatments using the composites of synthesized NPs were conducted to determine their efficiency at removing methylene blue dye from water. Methylene blue dye was photodegraded by exposing it to the synthesized NCs in the presence of UV and visible light. Some characteristics of dye degradation, such as concentration of the sample and contact duration, were assessed for their effect on dye disintegration. This study suggests that the prepared material could be effectively used as a photocatalyst for wastewater treatment and other related environmental applications.

Supplementary Materials: The following supporting information can be downloaded at: <https://www.mdpi.com/article/10.3390/separations10030200/s1>, Figure S1. Pictorial description of synthesis steps for Mn₃O₄ NPs; Figure S2. Pictorial description of synthesis steps for NiO NPs; Figure S3. Pictorial description of Mn₃O₄/NiO nanocomposite formation; Figure S4. Calibration curve of diluted stock solution; Figure S5. Adsorption capacity of MB dye Vs. time in dark; Figure S6. Remaining concentration of dye Vs. time in-terval; Table S1. XRD measurement of Mn₃O₄ NPs; Table S2. XRD measurement of NiO NPs; Table S3. XRD measurement of nanocomposite Mn₃O₄:NiO (1:1) and Table S4. XRD measurement of nanocomposite Mn₃O₄/NiO (3:1).

Author Contributions: Conceptualization, K.M., S.S.B., M.F. and A.D.C.; Methodology, K.M., S.M., M.A.B. and S.N.U.S.B.; Software, S.M. and A.D.C.; Validation, S.A.K. and M.F.; Formal analysis, S.M., M.A.B. and S.J.G.; Investigation, A.A.S., M.F. and S.N.U.S.B.; Resources, S.A.K., A.A.S., M.A.B. and M.N.B.J.; Data curation, S.A.K., M.F. and S.N.U.S.B.; Writing—original draft, K.M. and M.N.B.J.; Writing—review & editing, J.A., A.A.S., S.S.B. and S.J.G.; Supervision, J.A. and S.S.B.; Project administration, J.A., A.A.S., S.S.B., A.D.C. and S.J.G.; Funding acquisition, S.J.G. and M.N.B.J. All authors have read and agreed to the published version of the manuscript.

Funding: This study was funded by the Princess Nourah bint Abdulrahman University Researchers Supporting Project number (PNURSP2023R108), Princess Nourah bint Abdulrahman University, Riyadh, Saudi Arabia.

Data Availability Statement: Not Applicable.

Acknowledgments: This research project was supported by the Princess Nourah bint Abdulrahman University Researchers Supporting Project number (PNURSP2023R108), Princess Nourah bint Abdulrahman University, Riyadh, Saudi Arabia.

Conflicts of Interest: The authors declare no conflict of interest.

References

1. Ibrahim, R.K.; Hayyan, M.; AlSaadi, M.A.; Hayyan, A.; Ibrahim, S. Environmental application of nanotechnology: Air, soil, and water. *Environ. Sci. Pollut. Res.* **2016**, *23*, 13754–13788. [[CrossRef](#)] [[PubMed](#)]
2. Obey, G.; Adelaide, M.; Ramaraj, R. Biochar derived from non-customized matamba fruit shell as an adsorbent for wastewater treatment. *J. Bioresour. Bioprod.* **2022**, *7*, 109–115. [[CrossRef](#)]
3. Linley, S.; Thomson, N.R. Environmental Applications of Nanotechnology: Nano-enabled Remediation Processes in Water, Soil and Air Treatment. *Water Air Soil Pollut.* **2021**, *232*, 1–50. [[CrossRef](#)]
4. Tom, A.P. Nanotechnology for sustainable water treatment—A review. *Mater. Today Proc.* **2021**. [[CrossRef](#)]
5. Emmanuel, S.S.; Adesibikan, A.A.; Saliu, O.D. Phytogenically bioengineered metal nanoarchitecture for degradation of refractory dye water pollutants: A pragmatic minireview. *Appl. Organomet. Chem.* **2023**, *37*, e6946. [[CrossRef](#)]
6. Morin, N.; Eric, C.; Guorui, L.; Balaram, V.; Rita, A.; Ribeiro, L. Worldwide cases of water pollution by emerging contaminants: A review. *Environ. Chem. Lett.* **2022**, *20*, 2311–2338. [[CrossRef](#)]
7. Bhatti, M.A.; Shah, A.A.; Almani, K.F.; Tahira, A.; Chalangar, S.E.; dad Chandio, A.; Nur, O.; Willander, M.; Ibupoto, Z.H. Efficient photo catalysts based on silver doped ZnO nanorods for the photo degradation of methyl orange. *Ceram. Int.* **2019**, *45*, 23289–23297. [[CrossRef](#)]
8. Jjagwe, J.; Olupot, P.W.; Menya, E.; Kalibbala, H.M. Synthesis and Application of Granular Activated Carbon from Biomass Waste Materials for Water Treatment: A Review. *J. Bioresour. Bioprod.* **2021**, *6*, 292–322. [[CrossRef](#)]
9. Ziemba, C.; Larivé, O.; Reynaert, E.; Huisman, T.; Morgenroth, E. Linking transformations of organic carbon to post-treatment performance in a biological water recycling system. *Sci. Total Environ.* **2020**, *721*, 137489. [[CrossRef](#)]
10. Gallareta-Olivares, G.; Rivas-Sanchez, A.; Cruz-Cruz, A.; Hussain, S.M.; González-González, R.B.; Cárdenas-Alcaide, M.F.; Iqbal, H.M.; Parra-Saldívar, R. Metal-doped carbon dots as robust nanomaterials for the monitoring and degradation of water pollutants. *Chemosphere* **2023**, *312*, 137190. [[CrossRef](#)]
11. Jiang, S.; Yang, W. Template-Free Synthesis of Magnetic La-Mn-Fe Tri-Metal Oxide Nanofibers for Efficient Fluoride Remediation: Kinetics, Isotherms, Thermodynamics and Reusability. *Polymers* **2022**, *14*, 5417. [[CrossRef](#)] [[PubMed](#)]
12. Wang, J.; Sun, Y.; Zhao, X.; Chen, L.; Peng, S.; Ma, C.; Duan, G.; Liu, Z.; Wang, H.; Yuan, Y.; et al. A poly (amidoxime)—Modified MOF macroporous membrane for high—Efficient uranium extraction from seawater. *e-Polymers* **2022**, *22*, 399–410. [[CrossRef](#)]
13. Zhou, G.; Li, S.; Niu, C.; Wang, Q.; Zhang, X.; Meng, Q.; Li, L. Fir sawdust as a low—Cost and easily recyclable adsorbent: Efficient removal of Pb (II), Cu (II), and Zn (II) contaminants from wastewater. *Environ. Sci. Pollut. Res.* **2023**, 1–15. [[CrossRef](#)]
14. Liu, S.; Wang, M.; He, Y.; Cheng, Q.; Qian, T.; Yan, C. Covalent organic frameworks towards photocatalytic applications: Design principles, achievements, and opportunities. *Coord. Chem. Rev.* **2023**, *475*, 214882. [[CrossRef](#)]
15. Bukhari, S.N.; Shah, A.A.; Bhatti, M.A.; Tahira, A.; Channa, I.A.; Shah, A.K.; Chandio, A.D.; Mahdi, W.A.; Alshehri, S.; Ibupoto, Z.H.; et al. Psyllium-Husk-Assisted Synthesis of ZnO Microstructures with Improved Photocatalytic Properties for the Degradation of Methylene Blue (MB). *Nanomaterials* **2022**, *12*, 3568. [[CrossRef](#)] [[PubMed](#)]
16. Ujjan, Z.A.; Bhatti, M.A.; Shah, A.A.; Tahira, A.; Shaikh, N.M.; Kumar, S.; Mugheri, A.Q.; Medany, S.S.; Nafady, A.; Alnjiman, F.; et al. Simultaneous doping of sulfur and chloride ions into ZnO nanorods for improved photocatalytic properties towards degradation of methylene blue. *Ceram. Int.* **2022**, *48*, 5535–5545. [[CrossRef](#)]
17. Shah, A.A.; Bhatti, M.A.; Tahira, A.; Chandio, A.D.; Channa, I.A.; Sahito, A.G.; Chalangar, E.; Willander, M.; Nur, O.; Ibupoto, Z.H. Facile synthesis of copper doped ZnO nanorods for the efficient photo degradation of methylene blue and methyl orange. *Ceram. Int.* **2020**, *46*, 9997–10005. [[CrossRef](#)]
18. Bhatti, M.A.; Almaani, K.F.; Shah, A.A.; Tahira, A.; Chandio, A.D.; Mugheri, A.Q.; Bhatti, A.L.; Waryani, B.; Medany, S.S.; Nafady, A.; et al. Low Temperature Aqueous Chemical Growth Method for the Doping of W into ZnO Nanostructures and Their Photocatalytic Role in the Degradation of Methylene Blue. *J. Clust. Sci.* **2022**, *33*, 1445–1456. [[CrossRef](#)]
19. Ouyang, W.-T.; Xiao, F.; Ou, L.-J.; He, W.-M. Green Photocatalytic Syntheses Using Water as Solvent/Hydrogen Source/Oxygen Source. *Curr. Opin. Green Sustain. Chem.* **2023**, *40*, 100760. [[CrossRef](#)]
20. Khan, S.; Hussain, A.; He, K.; Liu, B.; Imran, Z.; Ambreen, J.; Hassan, S.; Ahmad, M.; Batool, S.S.; Li, C. Tailoring the bandgap of Mn₃O₄ for visible light driven photocatalysis. *J. Environ. Manag.* **2021**, *293*, 112854. [[CrossRef](#)] [[PubMed](#)]
21. Jian, S.; Tian, Z.; Zhang, K.; Duan, G.; Yang, W.; Jiang, S. Hydrothermal Synthesis of Ce-doped ZnO Heterojunction Supported on Carbon Nanofibers with High Visible Light Photocatalytic Activity. *Chem. Res. Chin. Univ.* **2021**, *37*, 565–570. [[CrossRef](#)]

22. Nami, M.; Sheibani, S.; Rashchi, F. Photocatalytic performance of coupled semiconductor ZnO–CuO nanocomposite coating prepared by a facile brass anodization process. *Mater. Sci. Semicond. Process.* **2021**, *135*, 106083. [[CrossRef](#)]
23. Shah, A.A.; Chandio, A.D.; Sheikh, A.A. Boron doped ZnO nanostructures for photo degradation of methylene blue, methyl orange and rhodamine B. *J. Nanosci. Nanotechnol.* **2021**, *21*, 2483–2494. [[CrossRef](#)] [[PubMed](#)]
24. Bhatti, M.A.; Gilani, S.J.; Shah, A.A.; Channa, I.A.; Almani, K.F.; Chandio, A.D.; Halepoto, I.A.; Tahira, A.; Bin Jumah, M.N.; Ibupoto, Z.H. Effective removal of methylene blue by surface alteration of TiO₂ with Ficus Carica leaf extract under visible light. *Nanomaterials* **2022**, *12*, 2766. [[CrossRef](#)] [[PubMed](#)]
25. Osgouei, M.S.; Kamrani, N.; Fazli-Shokouhi, S.; Khatamian, M. Improved performance of Mn₃O₄-based nanocomposites in photocatalytic removal of methylene blue. *J. Alloys Compd.* **2022**, *902*, 163729. [[CrossRef](#)]
26. Shaikh, B.; Bhatti, M.A.; Shah, A.A.; Tahira, A.; Shah, A.K.; Usto, A.; Aftab, U.; Bukhari, S.I.; Alshehri, S.; Shah Bukhari, S.N.U.; et al. Mn₃O₄ @ ZnO Hybrid Material: An Excellent Photocatalyst for the Degradation of Synthetic Dyes including Methylene Blue, Methyl Orange and Malachite Green. *Nanomaterials* **2022**, *12*, 3754. [[CrossRef](#)] [[PubMed](#)]
27. Wu, S.; Lin, Y.; Hu, Y.H. Strategies of tuning catalysts for efficient photodegradation of antibiotics in water environments: A review. *J. Mater. Chem. A* **2021**, *9*, 2592–2611. [[CrossRef](#)]
28. Tholkappiyar, R.; Naveen, A.N.; Vishista, K.; Hamed, F. Investigation on the electrochemical performance of hausmannite Mn₃O₄ nanoparticles by ultrasonic irradiation assisted co-precipitation method for supercapacitor electrodes. *J. Taibah Univ. Sci.* **2018**, *12*, 669–677. [[CrossRef](#)]
29. Chen, R.; Yu, J.; Xiao, W. Hierarchically porous MnO₂ microspheres with enhanced adsorption performance. *J. Mater. Chem. A* **2013**, *1*, 11682–11690. [[CrossRef](#)]
30. Sukhdev, A.; Challa, M.; Narayani, L.; Manjunatha, A.S.; Deepthi, P.R.; Angadi, J.V.; Kumar, P.M.; Pasha, M. Synthesis, phase transformation, and morphology of hausmannite Mn₃O₄ nanoparticles: Photocatalytic and antibacterial investigations. *Heliyon* **2020**, *6*, e03245. [[CrossRef](#)]
31. Mannaa, M.A.; Qasim, K.F.; Alshorifi, F.T.; El-Bahy, S.M.; Salama, R.S. Role of NiO Nanoparticles in Enhancing Structure Properties of TiO₂ and Its Applications in Photodegradation and Hydrogen Evolution. *ACS Omega* **2021**, *6*, 30386–30400. [[CrossRef](#)]
32. Kannan, K.; Radhika, D.; Nikolova, M.P.; Sadasivuni, K.K.; Mahdizadeh, H.; Verma, U. Structural studies of bio-mediated NiO nanoparticles for photocatalytic and antibacterial activities. *Inorg. Chem. Commun.* **2020**, *113*, 107755. [[CrossRef](#)]
33. Kumar, V.P.; Pradeep, C.; Sha, M.M.R.; Radhakrishnan, P.; Mujeeb, A. Band-gap dependence of three-photon absorption in NiO nanoparticles synthesized at different calcination temperatures. *Opt. Laser Technol.* **2023**, *158*, 108809. [[CrossRef](#)]
34. Bhat, S.A.; Zafar, F.; Mondal, A.H.; Kareem, A.; Mirza, A.U.; Khan, S.; Mohammad, A.; Haq, Q.M.R.; Nishat, N. Photocatalytic degradation of carcinogenic Congo red dye in aqueous solution, antioxidant activity and bactericidal effect of NiO nanoparticles. *J. Iran. Chem. Soc.* **2020**, *17*, 215–227. [[CrossRef](#)]
35. Şahin, B.; Aydin, R.; Cetin, H. Tuning the morphological, structural, optical and dielectric properties of hausmannite (Mn₃O₄) films by doping heavy metal lead. *Superlattices Microstruct.* **2020**, *143*, 106546. [[CrossRef](#)]
36. Ramezanpour, S.; Sheikhshoae, I.; Khatamian, M. Synthesis, characterization and photocatalytic properties of V-doped Mn₃O₄ nanoparticles as a visible light-activated photocatalyst. *J. Mol. Liq.* **2017**, *231*, 64–71. [[CrossRef](#)]
37. Koe, W.S.; Lee, J.W.; Chong, W.C.; Pang, Y.L.; Sim, L.C. An overview of photocatalytic degradation: Photocatalysts, mechanisms, and development of photocatalytic membrane. *Environ. Sci. Pollut. Res.* **2020**, *27*, 2522–2565. [[CrossRef](#)] [[PubMed](#)]
38. Raj, B.G.S.; Asiri, A.M.; Wu, J.J.; Anandan, S. Synthesis of Mn₃O₄ nanoparticles via chemical precipitation approach for supercapacitor application. *J. Alloys Compd.* **2015**, *636*, 234–240. [[CrossRef](#)]
39. Bonomo, M. Synthesis and characterization of NiO nanostructures: A review. *J. Nanopart* **2018**, *20*, 222. [[CrossRef](#)]
40. Raj, R.A.; AlSalhi, M.S.; Devanesan, S. Microwave-assisted synthesis of nickel oxide nanoparticles using Coriandrum sativum leaf extract and their structural-magnetic catalytic properties. *Materials* **2017**, *10*, 460. [[CrossRef](#)]
41. Zhang, Y.; Fu, F.; Li, Y.; Zhang, D.; Chen, Y. One-step synthesis of Ag@TiO₂ nanoparticles for enhanced photocatalytic performance. *Nanomaterials* **2018**, *8*, 1032. [[CrossRef](#)]
42. Ashraf, M.A.; Liu, Z.; Peng, W.X.; Jermsttiparsert, K.; Hosseinzadeh, G.; Hosseinzadeh, R. Combination of sonochemical and freeze-drying methods for synthesis of graphene/Ag-doped TiO₂ nanocomposite: A strategy to boost the photocatalytic performance via well distribution of nanoparticles between graphene sheets. *Ceram. Int.* **2020**, *46*, 7446–7452. [[CrossRef](#)]
43. Onkani, S.P.; Diagboya, P.N.; Mtunzi, F.M.; Klink, M.J.; Olu-Owolabi, B.I.; Pakade, V. Comparative study of the photocatalytic degradation of 2-chlorophenol under UV irradiation using pristine and Ag-doped species of TiO₂, ZnO and ZnS photocatalysts. *J. Environ. Manag.* **2020**, *260*, 110145. [[CrossRef](#)] [[PubMed](#)]
44. Khatri, A.; Rana, P.S. Visible light assisted photocatalysis of Methylene Blue and Rose Bengal dyes by iron doped NiO nanoparticles prepared via chemical co-precipitation. *Phys. B Condens. Matter* **2020**, *579*, 411905. [[CrossRef](#)]
45. Jdidi, R.; Krifa, I.; Saadaoui, K.; Selma, H.B.; Krifa, H. Métastase méningée révélatrice d'un cancer du sein. *Neurochirurgie* **2020**, *66*, 325. [[CrossRef](#)]
46. Li, N.; He, M.; Lu, X.; Liang, L.; Li, R.; Yan, B.; Chen, G. Enhanced norfloxacin degradation by visible-light-driven Mn₃O₄/γ-MnOOH photocatalysis under weak magnetic field. *Sci. Total Environ.* **2021**, *761*, 143268. [[CrossRef](#)] [[PubMed](#)]
47. Shaik, M.R.; Syed, R.; Adil, S.F.; Kuniyil, M.; Khan, M.; Alqahtani, M.S.; Shaik, J.P.; Siddiqui, M.R.H.; Al-Warthan, A.; Sharaf, M.A.; et al. Mn₃O₄ nanoparticles: Synthesis, characterization and their antimicrobial and anticancer activity against A549 and MCF-7 cell lines. *Saudi J. Biol. Sci.* **2021**, *28*, 1196–1202. [[CrossRef](#)]

48. Alagiri, M.; Ponnusamy, S.; Muthamizhchelvan, C. Synthesis and characterization of NiO nanoparticles by sol-gel method. *J. Mater. Sci. Mater. Electron.* **2012**, *23*, 728–732. [[CrossRef](#)]
49. Shaik, D.P.M.D.; Rosaiah, P.; Hussain, O.M. Supercapacitive properties of Mn₃O₄ nanoparticles synthesized by hydrothermal method. *Mater. Today Proc.* **2016**, *3*, 64–73. [[CrossRef](#)]
50. Ristig, S.; Cibura, N.; Strunk, J. Manganese Oxides in Heterogeneous (Photo)Catalysis: Possibilities and Challenges. *Green* **2015**, *5*, 23–41. [[CrossRef](#)]

Disclaimer/Publisher's Note: The statements, opinions and data contained in all publications are solely those of the individual author(s) and contributor(s) and not of MDPI and/or the editor(s). MDPI and/or the editor(s) disclaim responsibility for any injury to people or property resulting from any ideas, methods, instructions or products referred to in the content.